3D Surface Reconstruction for Robotic Body Parts with Artificial Skins

Philipp Mittendorfer and Gordon Cheng

Abstract— In this paper, we present a new approach to reconstruct the 3D surface of robotic body parts equipped with artificial skins. We do so by fusing static knowledge on the shape, size and tessellation capabilities of the uniform cell our skin consists of, together with dynamic knowledge on its neighbors and measurements from its orientation sensor – a 3-axis accelerometer. Our approach makes it possible to reconstruct the 3D surface of robotic body parts equipped with a patch of skin in a very short time, providing the location and orientation of every unit in a patch relative to an automatically chosen origin on the patch, utilizing no external sensors and only robot independent information. We show experimental results on the 3D reconstruction of different skin patches.

I. INTRODUCTION

A. Motivation

Artificial skins provide direct feedback on the interaction of a robot – with itself or the environment. But without knowledge on the location/orientation of the sensors, and the shape of the surface, this feedback is meaningless. Deploying high resolution, whole body artificial skins on a robot, it will no longer be feasible to manually provide the complete location information. A manual process would be error prone, time consuming and inhibit the robot to autonomously cope with system changes and/or failure. It is thus desirable that the robot takes advantage of its own sensors and actuators, to calibrate itself in an acceptable amount of time, with little or no external support. To be able to transfer artificial skin hardware and software in between a variety of robots, the artificial skin system should only utilize common, but no robot specific a-priori knowledge, and impose little constraints on the robotic platform at hand.

B. Related Works

Spatial calibration of robotic body parts with artificial skins relates to the more general topic of *body schema in robotics*, which has been recently reviewed in depth in [1]. Here, we only highlight some of the related works.

In [2] a simulated robot visually learns the local kinematics of its hand. It then probes the position of tactile sensors on its face through the known hand position. Such an approach is limited to the reachable range and the accuracy of the local kinematics. In [3] De Prete *et al.* utilize a force/torque sensor in the upper arm of an iCub robot and a completely initialized kinematic chain, in order to estimate the location of skin force cells on the lower arm or hand, touching an external point probe. The approach fails when there is no force torque sensor in the given kinematic chain,

P. Mittendorfer and G. Cheng are with the Institute for Cognitive Systems, Technische Universität München, Karlstrasse 45/II, 80333 Munich, Germany Email: see http://www.ics.ei.tum.de/

Fig. 1. 3D Reconstruction of a skin patch placed on a KUKA LWR arm

preceding the body part under evaluation. In [4] a simulated baby body performs random movements in water, extracting topological structures with spatio-temporal correlation. This approach has been extended to provide 3D sensor position estimates [5]. Modayil uses high correlations, limited to k-nearest neighbors, to establish local distance constraints. A global optimization algorithm then unfolds the 3D space, maximizing the unconstrained sensor distances. Implicitly given a global shape, the estimate only vaguely resembles the original. Hoshi *et al.* utilize a fixed lattice structure of rigid links, equipped with triaxial accelerometers, to reconstruct the shape of a cloth-like sheet [6]. As the missing yaw angles are only estimated from assumptions on the elemental loops of the lattice, this accelerometer based approach suffers from singular configurations. Hoshi *et al.* extended the sensing capabilities of each link by a triaxial magnetometer [7], which can be considered infeasible for an artificial skin for a robot. Besides cost and space constraints, metallic structures and the electromagnetic noise distort the magnetic field close to every robot. Additionally, a fixed lattice grid also does not account for the flexibility of placing skin on a robot.

C. Our Approach

In this paper, we present a new approach to reconstruct the 3D surface of robotic body parts equipped with artificial skins (please see Fig. 1). We do so by fusing static knowledge on the shape, size and tessellation capabilities of the uniform unit cells our skin consist of (please refer to [8]) together with dynamic knowledge about its neighbors, and measurements from its orientation sensor – a 3-axis accelerometer. Our approach makes it possible to reconstruct the 3D surface of robotic body parts equipped with a patch of skin in a very short time, providing the location and orientation of every unit in a patch relative to an automatically chosen origin on the patch. In comparison to [6] our approach does not suffer from singularities in the rotation estimation.

Algorithm 1 3D Reconstruction of multiple skin patches

1: Detection of (U) available sensor units
2: Creation of a skin graph with (U) vertices
3: Exploration of unit network neighbors = neighbor list
4: Creation of directed port edges from neighbor list
5: Deletion of non-direct edges e.g. across body parts
6: Analysis of connected components = skin patches
7: **while** reconstruction loop **do**
8:     Sampling of gravity vectors in multiple poses (P)
9:     Estimation of edge rotations from gravity and port vectors
10:     Calculation of edge weights from estimation errors
11:     Find unit with shortest accumulated path for every patch
12:     Set these units as patch origins and memorize paths
13:     Default position and orientation of patch origins
14:     Update remaining unit orientations along calculation paths
15:     Update remaining unit positions along calculation paths
16: **end while**

We sample a complementary set of gravity vectors, actively or passively driving the robotic body parts into a variable number of different poses, while the skin remains undeformed. Our approach explicitly makes use of the intelligent networking capabilities of our artificial skin, able to explore the connectivity in between the nearest neighbors. Shifting the problem to graph theory and applying local, instead of global optimization the system can quickly adapt to changes, e.g. delete non-physical relations when body structure information becomes available (please refer to [9]). Utilizing no external sensors, and only little robot independent a-priori knowledge, the algorithms can be quickly transferred between robots. This touchless skin calibration approach saves time and enables fast initial or re-calibration.

II. SYSTEM DESCRIPTION

In this section, we first describe our artificial skin. We continue with a mathematical formulation of the problem, state our assumptions and present our solution. Finally, we address the scalability of our approach.
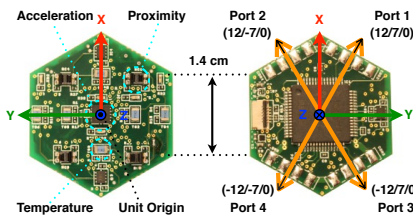
A. Artificial Skin

Fig. 2.   The sensor unit – uniform building block of the artificial skin

Our artificial skin builds from thin, hexagonal shaped, rigid unit cells (see Fig. 2) placed next to each other in a deformable elastomer mold (see Fig. 1). In comparison to rhomboids and triangles, we consider the hexagonal unit shape optimal for a uniform surface sensor network (see [8] for details). Every sensor unit (SU) features a set of multi-modal sensors on the front side, emulating human cues of touch – such as light touch, temperature and vibration

(refer to [10]). In this paper, we make use of the triaxial accelerometer – a BOSCH BMA150 – set at $\pm 2g$ range and $1kHz$ output rate. A local controller on the back side of every SU allows to locally convert, pre-process and forward sensor signals, and to organize an arbitrary network of units. Neighboring units are connected through four 4-wire data and power ports (see Fig. 2), each providing a bidirectional $12Mbit/s$ data link. Currently, only specific port combinations can be connected, in order to obey the port polarity pattern. At least one boundary port of a skin patch (SP), defined as a closely connected network of neighboring units, has to be connected to a computer interface. Executing an automated network exploration algorithm (see result in Fig. 3) the SU network discovers all (bidirectionally) available communication ports, sets up optimal routing pathways to the computer, distributes unique IDs and explores the network neighbors on every port. The position and orientation of the sensors on a SU, the size of the hexagonal shape and the port vectors, are known and static in respect to the local SU coordinate system.
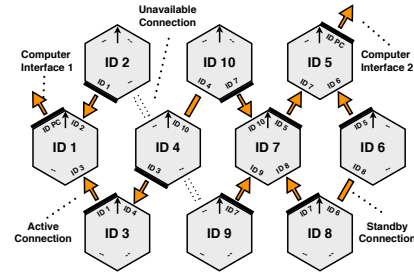

Fig. 3.   Automatic network exploration utilizing local communication

B. Problem Formulation

Our aim is to efficiently estimate the relative position and orientation of uniform sensor units (SU), distributed on the surface of robotic body parts, utilizing static a-priori and dynamically generated on-line knowledge.
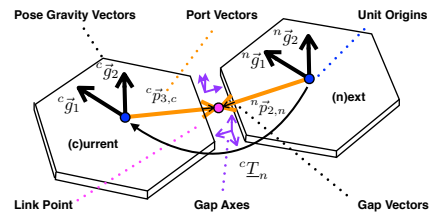

Fig. 4.   Model of the elastomer link in between two sensor units

As our artificial skin builds from an instantiation of the same thin rigid unit cell, rigid body transformations, featuring a rotation ${}^c\underline{R}_n$ and a translation ${}^c\vec{t}_n$, adequately describe the connection in between two neighboring SUs n and c (see Fig. 4). No scaling, shearing, reflection or projection takes place in between the uniform unit cells:

$$ {}^c\underline{T}_n = \begin{bmatrix} {}^c\underline{R}_n & {}^c\vec{t}_n \\ \underline{0} & 1 \end{bmatrix} \tag{1} $$

We further assume that the link in between two units n and c, directly connected through port l_c and l_n, can be approximated, setting the link point of the extended port vectors $^c\vec{p}_{l_c,c}$ and $^n\vec{p}_{l_n,n}$ equal in common coordinates:

$$^c\underline{T}_n \cdot {}^n\vec{p}_{l_n,n} \equiv {}^c\vec{p}_{l_c,c} \qquad (2)$$

This assumption is based on specific properties of our artificial skin: 1) artificial skin cells do not overlap; 2) a dense tessellation of thin hexagonal shaped unit cells on a surface, constrains the local placement and alignment of each cell; 3) ports have to be closely placed and initially aligned, to be directly connected; 4) the average gap size for a tessellation is known a-priori; 5) the translational component of a relatively small elastomer gap in between thin, rigid hexagonal cells can be neglected; 6) the point of rotation of the elastomer gap is approximately in its center. Based on these assumptions, we can neglect the change of the small gap vectors (see Fig. 4) and add half of the known gap size directly to each port vector - forming the four presented extended port vectors $^u\vec{p}_{l_u,u}$, known in unit u coordinates. Combining (1) and (2) leads to:

$$^c\vec{t}_n = {}^c\vec{p}_{l_c,c} - {}^c\underline{R}_n \cdot {}^n\vec{p}_{l_n,n} \qquad (3)$$

This shows that the relative translation $^c\vec{t}_n$ can be calculated from the relative rotation $^c\underline{R}_n$ and the connected ports. We utilize knowledge from the network exploration to find directly connected ports and measurements from the unit gravity vectors to estimate the relative rotation. When all local transformations in a skin patch (SP) are known, the orientation and position of every SU u, relative to a chosen origin unit o, can be calculated as kinematic chain between u and o, with a variable number of units x in between:

$$^o\underline{T}_u = {}^o\underline{T}_x \cdot \ldots \cdot {}^x\underline{T}_u \qquad (4)$$

An error estimate allocated to every local transformation allows to minimize the inherently accumulated error, searching for an optimal kinematic chain for every skin patch. The shape and size of the unit, as well as the position and orientation of every sensor on a unit, are known in unit coordinates. With Equation (4), it is possible to transform these into common skin patch coordinates. This allows the reconstruction of the partial shape of the carrier object, the surface of the skin patch and the orientation and location of every sensor in it, relative to the origin of each skin patch.
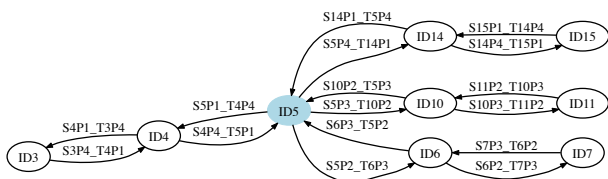
C. Problem Solution

Fig. 5.   Partial visualization of the X17 skin patch graph with GraphViz

1) **Representation as Graph:** We found that graph theory (here implemented with BGL[1]) provides an adequate representation for our artificial skin, and methods to efficiently handle arbitrary configurations of sensor units (SU). We begin with parsing the result of the automatic network exploration (refer to II-A) into an empty graph (refer to Alg. 1), attaching a property map to the graph, with a variable for the number of skin patches and a vector to memorize the origin of each skin patch. For every sensor unit we create a vertex, attaching a property map with its unique ID and placeholders for its skin patch ID, relative orientation matrix and position vector. For every neighbor, in the list of network neighbors, we create a directed edge, attaching a property map with the ID of the source and the target, as well as the source port and the target port, and placeholders for the relative rotation matrix and the weight related to the estimation error. As all available connections are bidirectional, each adds two edges (see Fig. 5). For the 3D reconstruction of skin patches, only close connections are of interest (refer to II-B). All others edges need to be deleted or muted. Here, we implemented two methods: 1) we delete edges to the computer interfaces, acting like units with top of the range IDs; 2) we delete edges in between different body parts (given knowledge from [8]), as so far, these can only be connected by long cables. For the next steps, the relative edge rotation estimation must be complete for all edges (refer to II-C.2). First, we perform a connected components algorithm on the whole graph. This algorithm returns the number of skin patches S and assigns every unit to a patch s. Next, we search the unit with the shortest accumulated path for every skin patch, based on a Dijkstra shortest path algorithm, and set it as origin o_s of the patch. As the positions $^w\vec{t}_{o_s}$ and orientations $^w\underline{R}_{o_s}$ of the skin patch origins are not defined, we default them to:

$$^w\vec{t}_{o_s} = \vec{0} \text{ and } ^w\underline{R}_{o_s} = \underline{I}, \ s \in \{1, ..., S\} \qquad (5)$$

Starting from each origin o_s, we then propagate along the shortest paths and update all relative unit orientations $^{o_s}\underline{R}_u$ and positions $^{o_s}\vec{t}_u$ along the kinematic chain:

$$^{o_s}\underline{R}_n = {}^{o_s}\underline{R}_c \, {}^c\underline{R}_n \qquad (6a)$$
$$^{o_s}\vec{t}_n = {}^{o_s}\vec{t}_c + {}^{o_s}\underline{R}_c \, {}^c\vec{t}_n \qquad (6b)$$

2) **Relative Rotation Estimation:** The rotational component $^c\underline{R}_n$ of the transformation $^c\underline{T}_n$ in between two directly connected units n and c combines two subcomponents: 1) the $\frac{2\pi}{6}$ repetitive initial port alignment of the hexagonal tessellation; 2) the deformation of the elastomer gap, simplified as rotation around the link point (see Fig. 4). Due to Equation (3) both can be estimated at the same time. However, it is possible to add specific additional knowledge, in case a subcomponent is not fully defined, which we will show later. We estimate the rotation $^c\underline{R}_n$ based on

[1]J. G. Siek and L. Q. Lee and A. Lumsdaine, "The Boost Graph Library", Addison-Wesley, 2001, version 1.4.9

measurements of the time t dependent unit gravity vectors ${}^c\vec{g}_c(t)$ and ${}^n\vec{g}_n(t)$ with the triaxial accelerometer on every unit. This is possible as the gravitational field ${}^w\vec{g}({}^w\vec{r} + {}^w\vec{s})$ in world coordinates w, for a robot on the earth surface (${}^w\vec{r} = 6371km$, $M = 5.9 \times 10^{24}kg$, $G = 6.7 \times 10^{-11}\frac{m^3}{kg \cdot s^2}$), is independent of the sample point (${}^w\vec{s} << {}^w\vec{r}$), the mass of the robot ($m << M$) and time t.

$$
{}^w\vec{g}({}^w\vec{r} + {}^w\vec{s}) = -\frac{G(M+m)}{|{}^w\vec{r} + {}^w\vec{s}|^3}({}^w\vec{r} + {}^w\vec{s}) \approx {}^w\vec{g} \qquad (7)
$$

The relative (time dependent) rotation matrix ${}^c\underline{R}_n(t)$ thus directly links the two local gravity vectors ${}^c\vec{g}_c(t)$ and ${}^n\vec{g}_n(t)$:

$$
{}^c\underline{R}_n(t){}^n\vec{g}_n(t) = {}^c\vec{g}_c(t) \qquad (8)
$$

As described in [6], a single measurement of the gravity vectors is not sufficient to estimate the relative orientation of rigid bodies. Here, we present a method to combine a variable number of measurements of the gravity vectors ${}^c\vec{g}_{c,p}$ and ${}^n\vec{g}_{n,p}$ in P different poses p, to gain the missing complementary information. We therefore actively or passively drive the skin patches in different poses in between two measurements. Active means that the robot actuates a related, rotatory joint itself. Whereas passive specifies that the operator changes the whole robot orientation or forces a related rotatory joint to move. The method assumes that the relative rotation ${}^c\underline{R}_n(t)$ changes only little over the lifetime T of the reconstruction:

$$
{}^c\underline{R}_n(t) \approx {}^c\underline{R}_n, t \in [0, T] \qquad (9)
$$

This (quasi) rigid body assumption makes it possible to continuously generate new sets of gravity vectors, changing the orientation ${}^b\underline{R}_w(t)$ of the body part b the skin patch is mounted on, in time t:

$$
{}^c\underline{R}_n{}^n\underline{R}_w(t){}^w\vec{g} = {}^c\underline{R}_w(t){}^w\vec{g} \qquad (10a)
$$
$$
{}^n\underline{R}_w(t) \equiv {}^c\underline{R}_w(t) \equiv {}^b\underline{R}_w(t) \qquad (10b)
$$

Complementary information specifies that the following system of equations, to solve the nine unknown elements of the 3×3 rotation matrix ${}^c\underline{R}_n$, has to be determined:

$$
{}^c\underline{R}_n{}^n\vec{g}_{n,p} = {}^c\vec{g}_{c,p} \qquad (3 \times P) \qquad (11a)
$$
$$
det({}^c\underline{R}_n) = 1 \qquad (1) \qquad (11b)
$$
$$
{}^c\underline{R}_n^T = {}^c\underline{R}_n^{-1} \qquad (3) \qquad (11c)
$$

Equation (11a) can provide up to 9 independent equations based on $P = 3$ orthogonal gravity vectors:

$$
{}^u\vec{g}_{u,1}^T{}^u\vec{g}_{u,2} = {}^u\vec{g}_{u,1}^T{}^u\vec{g}_{u,3} = {}^u\vec{g}_{u,2}^T{}^u\vec{g}_{u,3} \equiv 0, u \in \{n, c\} \quad (12)
$$

Given the additional properties of the rotation matrix, defined in Equations (11b) and (11c), it is sufficient to provide the system with a set of $P = 2$ independent gravity measurements, to maintain an overdetermined system.

Certain rotations of the body part, in order to reach new poses, are excluded to obtain independent equations in (11a). Rotations around the gravity vector itself or π repetitive rotations around any axis, provide linearly dependent equations. We decided to utilize a constrained general solution of the procrustes problem[2], to find a rotation matrix ${}^c\underline{R}_n$ that closely maps a variable set ${}_n\underline{N}^{P \times 3}$ of P gravity vectors ${}^n\vec{g}_{n,p}$ to a variable set ${}_c\underline{C}^{P \times 3}$ of P gravity vectors ${}^c\vec{g}_{c,p}$. The actual solution of the mapping is thus shifted to a singular value decomposition of the two sample sets ${}_n\underline{N}$ and ${}_c\underline{C}$:

$$
{}_{nc}\underline{U}\,{}_{nc}\underline{\Sigma}\,{}_{nc}\underline{V}^T = svd\left({}_n\underline{N}^T{}_c\underline{C}\right) \qquad (13)
$$

The rotation matrix ${}^c\underline{R}_n$ builds from the left singular vectors in ${}_{nc}\underline{U}$, the right singular vectors in ${}_{nc}\underline{V}$ and ${}_{nc}\underline{\Sigma}'$:

$$
{}^c\underline{R}_n = {}_{nc}\underline{U}\,{}_{nc}\underline{\Sigma}'\,{}_{nc}\underline{V}^T \qquad (14)
$$

Sigma ${}_{nc}\underline{\Sigma}'$ is a 3×3 identity matrix $\underline{I}^{3 \times 3}$ with the location of the lowest singular value at $(3, 3)$ replaced with the determinant $det({}_{nc}\underline{U}{}_{nc}\underline{V}^T)$, in order to enforce ${}^c\underline{R}_n$ to be a special orthogonal matrix:

$$
{}_{nc}\underline{\Sigma}' = \begin{pmatrix} 1 & 0 & 0 \\ 0 & 1 & 0 \\ 0 & 0 & det({}_{nc}\underline{U}{}_{nc}\underline{V}^T) \end{pmatrix} \qquad (15)
$$

We only utilize the original singular values ${}_{nc}\sigma_1 \geq {}_{nc}\sigma_2 \geq {}_{nc}\sigma_3$ in ${}_{nc}\underline{\Sigma}$ in order to evaluate the quality of the estimation. In the following calculations we assume that all measured gravity vectors are normalized:

$$
|\vec{g}| \equiv 1[g] \qquad (16)
$$

Deviations of $\vec{g}$ from the local constant $\frac{GM}{r^2}$ indicate additional effects with the accelerometer (see Equ. (18)). With the normalization, we make our approach independent of the local constant. The estimation of ${}^c\underline{R}_n$ itself is not affected by a normalization, as a rotation conserves the length of a vector. Here, we only differentiate in four estimation qualities, with the following edge weights ${}_{nc}w$:

$$
\begin{array}{llll}
\text{un-} & {}_{nc}\sigma_1 < 1, {}_{nc}\sigma_2 < 1 & {}_{nc}w = 3 & (17a) \\
\text{partially-} & {}_{nc}\sigma_1 \geq 1, {}_{nc}\sigma_2 < 1 & {}_{nc}w = 2 & (17b) \\
\text{fully-} & {}_{nc}\sigma_1 \geq 1, {}_{nc}\sigma_2 \geq 1, {}_{nc}\sigma_3 < 1 & {}_{nc}w = 1 & (17c) \\
\text{over-defined} & {}_{nc}\sigma_1 \geq 1, {}_{nc}\sigma_2 \geq 1, {}_{nc}\sigma_3 \geq 1 & {}_{nc}w = 1 & (17d)
\end{array}
$$

In case of an undefined or only partially defined estimation, it is not possible to completely estimate the rotational component around the link point in the elastomer gap. However, the alignment of the connected ports can still be enforced, appending a set of scaled (10% of unit length), correctly signed (incoming or outgoing) gap axes (see Fig. 4) to the data sets ${}_n\underline{N}$ and ${}_c\underline{C}$. The influence of the support axes vanishes when the gravity measurements (P unit vectors) are well defined, but help to stabilize the system output in un-

[2]P. H. Schonemann, "A generalized solution of the orthogonal Procrustes problem", Psychometrika 31, pp. 1-10, 1966

or partially defined cases. Finally, we wish to describe the sampling of the gravity vectors. We measure the the gravity vectors $^u\vec{g}_{u,p}$ of every unit u in a skin patch in different poses p with an accelerometer aligned with the unit origin. The accelerometer does not only measure a rotated version of the world gravity vector $^w\vec{g}$, but also the second time derivative of position of the unit origin, transformed from world $^w\vec{o}_u(t)$ into unit $^u\vec{o}_u(t)$ coordinates by the rigid body transformation $^u\underline{T}_{w,p}(t)$ of pose p:

$$^u\vec{a}_{u,p}(t) = \frac{d^2}{dt^2}\left(^u\underline{R}_{w,p}(t)^w\vec{o}_{u,p}(t) + {}^w\vec{t}_{u,p}(t)\right) + \\ + {}^u\underline{R}_{w,p}(t)^w\vec{g} \quad (18)$$

This shows that, in order to be able to extract the gravity vector from the accelerometer data, the skin patch has to maintain a static pose in world coordinates. We then average $K = 100$ subsequent samples at $1kHz$ in every pose p to decrease the influence of noise and vibrations on the robot:

$$^u\vec{g}_{u,p} = \frac{1}{K}\sum_{k=1}^{S} {}^u\vec{a}_{u,p}[k] \quad (19)$$

Sampling a pose p thus currently takes 100ms.

D. Scalability

Every time a new, e.g. scaled unit version has to be integrated, only the unit specific information must be updated. A smaller size of the unit cell naturally increases the number of consecutive transformations, which increases the potential for propagation errors. However, we think that the increasing number of alternate pathways, the decreasing influence of a single (local) transformation and the denser sampling of the surface will finally decrease the overall error. A higher number of unit cells, and their subsequent connections, will also increase robustness due to the manifold of network redundancies. Erroneous connections or units are automatically ignored during network calibration, only connected components are automatically labeled as patches. Shifting to flexible units, a smaller unit size would also allow to neglect the unit deformation and to continue with the rigid body assumption. As our approach only has to estimate the relative rotation in between units, it could be implemented with alternative sensors – e.g. direct 3D bending sensors in the gap. In order to save high level processing time, most of the relative computations can be shifted to the unit cells. Finding direct neighbors through the network exploration is a very fast method, it currently takes roughly $130ms$ to power up and explore $U = 31$ units – most of which is static waiting times. Still, we could generate edges with a different method, using e.g. informational distances, for an artificial skin that does not provide this feature. Regarding processing power our approach is efficient. The rotation estimation is calculated numerically with a singular value decomposition, while the graph algorithms have known complexity. All test patches shown in Section III can be reconstructed with $f \approx$ 10Hz, in our automatically refreshing single pose test mode (100ms sample time). Currently our approach is limited

to the reconstruction of skin patches. This is due to the unknown transformations in between skin patch origins.

III. EXPERIMENTS

In this section, we provide experimental results on the 3D reconstruction quality of exemplary test patches.
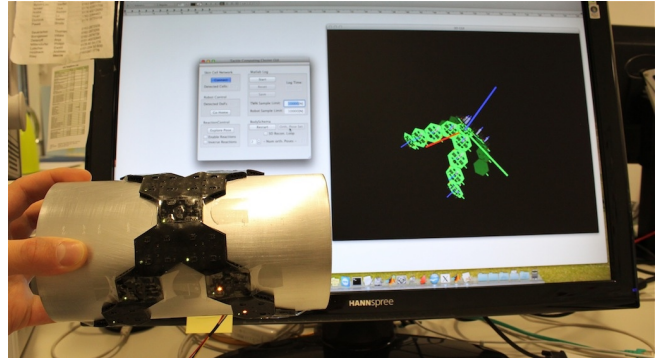

Fig. 6. 3D reconstruction of a cylindrical carrier with the X17 patch

1) **Shape Reconstruction:** In this experiment, we provide qualitative results on the reconstruction quality of a carrier object. To do this, we put a X-shaped skin patch, made from $U = 17$ sensor units, on a geometrically known object, an aluminium cylinder with a measured radius of $r_{\text{real}} = 50.1$mm (see Fig. 6). We sample a minimal set of gravity vectors in $P = 2$ orthogonal poses. The first pose with the cylinder standing on a desk, the second held by hand as depicted in Fig. 6, to account for vibrations. We then compare the generated point cloud $^{o_s}\vec{t}_u$ of the $U = 17$ unit origins u, with the ground truth – the parameterized cylinder surface. As we do neither exactly know the alignment of the x-shaped patch on the cylinder, nor its axis or a point on it, we start with a registration algorithm on the point cloud. We utilize the *fgcylinder* function of the LSGE[3] MATLAB library. Besides the point cloud, *fgcylinder* requires rough initial estimates on the cylinder axis ($^{o_s}\vec{h}_{\text{init}} = [0;1;0]$mm), the radius ($r_{\text{init}} = 15$mm) and one point on the axis ($^{o_s}\vec{b}_{\text{init}} = [0;0;-15]$mm), which we provide. Starting from this input, *fgcylinder* estimates the best fitting cylinder axis ($^{o_s}\vec{h}_{\text{est}} = [-0.02;1.00;0.01]$mm), radius ($r_{\text{est}} = 49.80$mm) and one point on the axis ($^{o_s}\vec{b}_{\text{est}} = [-3.11;1.21;-49.64]$mm), based on a least squares algorithm. Additionally, it provides an array $d_{\text{est}}[U]$ of the minimal radial distances, in between each of the U unit origins and the parameterized surface model (see Fig. 7). We utilize this array, along with the difference in between the real r_{real} and estimated r_{est} cylinder radii, in order to build a quantitative reconstruction error $\varepsilon_{\text{recon}}$ metric:

$$\triangle = r_{\text{est}} - r_{\text{real}} \quad (20)$$

$$\varepsilon_{\text{recon}} = \sqrt{\frac{1}{U}\sum_{u=1}^{U}\left(d_{\text{est}}[u] + \triangle\right)^2} \quad (21)$$

[3]"The least squares geometric elements library", EUROMET Repository of Software, version 0.7.6

For the experiment show in Fig. 6 we maintained a difference of $\triangle = -0.30$mm and an error of $\varepsilon_{\text{recon}} = 1.62$mm.

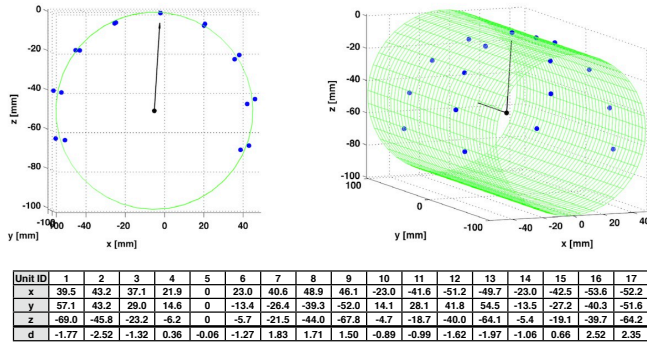| Unit ID	1	2	3	4	5	6	7	8	9	10	11	12	13	14	15	16	17
x	39.5	43.2	37.1	21.9	0	23.0	40.6	48.9	46.1	-23.0	-41.6	-51.2	-49.7	-23.0	-42.5	-53.6	-52.2
y	57.1	43.2	29.0	14.6	0	-13.4	-26.4	-39.3	-52.0	14.1	28.1	41.8	54.5	-13.5	-27.2	-40.3	-51.6
z	-69.0	-45.8	-23.2	-6.2	0	-5.7	-21.5	-44.0	-67.8	-4.7	-18.7	-40.0	-64.1	-5.4	-19.1	-39.7	-64.2
d	-1.77	-2.52	-1.32	0.36	-0.06	-1.27	1.83	1.71	1.50	-0.89	-0.99	-1.62	-1.97	-1.06	0.66	2.52	2.35

Fig. 7.   Comparison of the cylinder point cloud with ground truth

We did not take the thickness $f \approx 3.4$mm of the skin into account, statically modeled the elastomer gap as an extension of the according port vectors by half of the gap ($\frac{1.77}{2}$mm) and did not calibrate the triaxial accelerometers. We are aware that a selection of the unit origins, as sample points, is optimal for a concave surface like the cylinder, whereas points on the boundary of the rigid hexagonal shape would be optimal for a convex surface. With a decrease of the unit size, in comparison to the curvature of the robotic part, this will no longer be relevant.
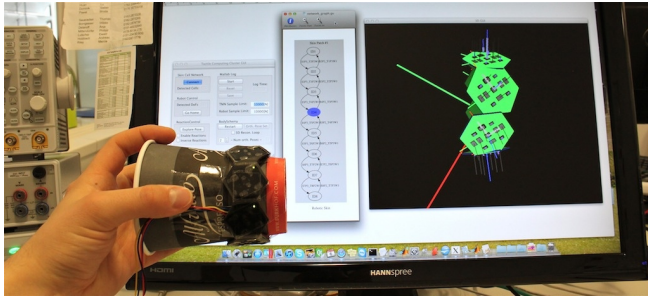

Fig. 8.   Closed loop reconstruction of a skin patch with 8 units

2) **Closed Loop Case:** In this experiment, we provide qualitative results on the closed loop test case. To do this, we place a patch of $U = 8$ units in the longest configuration - a straight line. We then tape the two unconnected ends closely together, forming a ring (see Fig. 8). In order to stabilize the shape between poses, we fix the patch on a paper cup. We then sample $P = 2$ orthogonal poses, one with the cup standing on the table, the other holding the cup by hand, to account for vibrations. Fig. 9 depicts the difference in between the link points ${}^{o_s}\vec{p}_{2,1}$ and ${}^{o_s}\vec{p}_{3,8}$ of the unconnected, but closely placed ports 2 and 3, in between the units with ID 1 and ID 8. In the given experiment the difference vector $\vec{\delta} = [-6.10; -2.36; 8.16]$mm has a length of $|\vec{\delta}| = 10.46$mm. Compared to the loop length $L = 222.28$mm of the 16 accumulated port vectors, the error is 4.71%. The curvature of the skin, and thus also the error of the simplified gap model, is higher then in the previous experiment. Every

gap is prone to a $360/8 = 45°$ rotation. The light cup also makes it difficult to hold the second pose manually stable. Both will be less problematic once we move onto the robot.
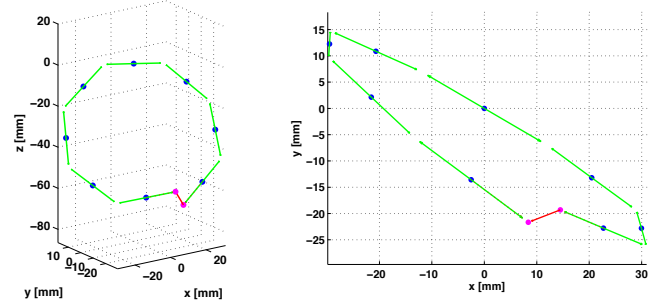

Fig. 9.   Deviation of link points in the closed loop experiment

IV. **CONCLUSION**

In this paper, we introduced a touch-less approach to reconstruct the 3D shape of robotic body parts, based on an internal observer with minimal a-priori information on the elemental unit cell of our skin. Our algorithm poses constraints on the design of the artificial skin and can currently only reconstruct patches of skin. Accounting for these limitations, our method provides a very fast (< 250ms) and sufficiently accurate ($< 5\%$ error) procedure to gain parts of the robot body schema - the shape of body parts and the relative orientation and position of sensors on them.

REFERENCES

[1] M. Hoffmann, H. G. Marques, A. H. Arieta, H. Sumioka, M. Lungarella, and R. Pfeifer, "Body schema in robotics: A review," *IEEE Transactions on Autonomous Mental Development*, vol. 2, no. 4, pp. 304–324, December 2010.

[2] S. Fuke, M. Ogino, and M. Asada, "Body image constructed from motor and tactile images with visual information," *International Journal of Humanoid Robotics*, vol. 4, no. 2, pp. 347–364, March 2007.

[3] A. D. Prete, S. Denei, L. Natale, F. Mastrogiovanni, F. Nori, G. Cannata, and G. Metta, "Skin spatial calibration using force/torque measurements," *IEEE/RSJ International Conference on Intelligent Robots and Systems*, pp. 3694–3700, September 2011.

[4] Y. Kuniyoshi, Y. Yorozu, Y. Ohmura, K. Terada, T. Otani, A. Nagakubo, and T. Yamamoto, "From humanoid embodiment to theory of mind," *Lecture Notes in Computer Science*, pp. 202–218, 2004.

[5] J. Modayil, "Discovering sensor space: Constructing spatial embeddings that explain sensor correlations," *IEEE 9th International Conference on Development and Learning*, pp. 120–125, 2010.

[6] T. Hoshi and H. Shinoda, "Gravity-based 3d shape measuring sheet," *SICE Annual Conference*, pp. 2126 – 2131, September 2007.

[7] ——, "3d shape measuring sheet utilizing gravitational and geomagnetic fields," *SICE Annual Conference*, pp. 915–920, 2008.

[8] P. Mittendorfer and G. Cheng, "Uniform cellular design of artificial robotic skin," *7th German Conference on Robotics*, pp. 145–149, May 2012.

[9] ——, "Open-loop self-calibration of articulated robots with artificial skins," *IEEE International Conference on Robotics and Automation*, pp. 4539–4545, May 2012.

[10] ——, "Humanoid multi-modal tactile sensing modules," *IEEE Transactions on Robotics*, vol. 27, no. 3, pp. 401–410, June 2011.